DOI: 10.1002/ejic.201000110

Luminescent $CaWO_4$:Tb^{3+}-Loaded Mesoporous Silica Composites for the Immobilization and Release of Lysozyme

Shanshan Huang,[a] Chunxia Li,[a] Piaoping Yang,[a] Cuimiao Zhang,[a] Ziyong Cheng,[a] Yong Fan,[a] and Jun Lin*[a]

Keywords: Immobilization / Luminescence / Mesoporous materials / Lanthanides / Bioinorganic chemistry

Luminescence-functionalized silica composites were synthesized by deposition of $CaWO_4$:Tb^{3+} nanoparticles onto mesoporous silica (MS) materials by a Pechini-type sol–gel process. The pristine mesoporous silica materials comprise rod-like and spherical SBA-15-type silica materials in micron size, hollow silica spheres of around 2–4 μm, and silica tubes with lengths of tens of micrometers. The X-ray diffraction (XRD), transmission electron microscopy (TEM), and N_2 adsorption/desorption results confirm that the composites still conserve regular mesopore structure after the incorporation of the $CaWO_4$:Tb^{3+} nanoparticles. These luminescent composites possessing suitable pore size, high BET surface area, and large pore volume ($> 1.0\ cm^3/g$) were studied as supports for immobilization of lysozymes. These composites show various lysozyme adsorption capacities at different solution pH values. $CaWO_4$:Tb^{3+}-loaded SBA-15-type composites and hollow spheres adsorb relatively high amounts (> 500 mg/g composite at a solution pH of 10.0) of lysozyme (LYZ). The different enzyme adsorption and release properties of these luminescent mesoporous silica materials make them good candidates for specific bioimmobilization hosts. The emission intensity of Tb^{3+} in the $CaWO_4$:Tb^{3+}@rod-like SBA-15 varies with the total released amount of LYZ, which enables the lysozyme release to be tracked by the change in the luminescence intensity.

Introduction

The immobilization of biomolecules on solid supports has been intensively studied because of their wide utilizations in enzymatic catalysis, separation, biosensors, and diagnosis.[1] Both inorganic and organic materials, such as controlled porous glass,[2] chitosan,[3] sol–gels,[4] microgels,[5] and porous carbon molecular sieves,[6] have been studied as supports for enzyme immobilization. The immobilization of enzymes on inorganic materials have been widely investigated because of the potential to improve the stability of enzymes under extreme conditions.[7] Among the inorganic materials, mesoporous silica (MS) materials have attracted much attention as promising supports for the immobilization of enzymes on the basis of their large surface area, tunable pore size and volume, and content of easily functionalized surface silanol groups.[8] Owing to their silicate inorganic framework, mesoporous silica materials are chemically and mechanically stable and resistant to microbial attack.[9]

The adsorption and separation of proteins and other biologically relevant molecules, such as amino acids, based on MS materials have been reported by many groups.[10] Silica materials functionalized by different chemical groups and multilayer shells enhanced the capacity or stability of enzymes.[11] Magnetic silica/iron oxide nanocomposites with mesostructure porosity were synthesized for immobilization of lysozymes.[12] The distinctive photophysical properties of trivalent lanthanide (Ln^{III}) ions, which emit line-like and easily recognizable luminescence spectra, open the way to applications in the bioanalysis field.[13] Mesoporous materials functionalized with photoluminescent compounds, especially those showing the red luminescence of Eu^{3+}, have potential applications in the fields of drug delivery, diagnosis, and therapy.[14] The extent of drug release can be monitored by the change in luminescence.

Herein, luminescence-functionalized silica composites were synthesized by deposition of $CaWO_4$:Tb^{3+} nanoparticles onto the MS materials by a Pechini-type sol–gel process. Rod-like and spherical SBA-15-type silica materials, mesoporous hollow spheres of around 2–4 μm, and silica tubes with lengths of tens of micrometers were chosen as matrices. These prepared silica materials possess large pore volumes and suitable pore sizes that are accessible for enzymes with large molecule size. The hen egg white lysozyme (LYZ), which has a prolate spheroid shape with two characteristic cross sections: a side of dimensions of roughly $3.0 \times 4.5\ nm^2$ and an end of dimensions of $3.0 \times 3.0\ nm^2$, was chosen as the model protein.[15] The isoelectric point (pI) of LYZ is around 11.[10f] The lysozyme adsorption behavior of these composites with different morphologies and mesopo-

[a] State Key Laboratory of Rare Earth Resource Utilization, Changchun Institute of Applied Chemistry, Chinese Academy of Sciences,
Changchun 130022, P. R. China
Fax: +86-431-85698041
E-mail: jlin@ciac.jl.cn

rous structures was investigated. These materials containing rare earth elements are photoluminescent, and the emission intensity of Tb^{3+} changes as a function of the total amount of lysozyme molecules released.

Results and Discussion

Structural and Morphological Properties

XRD

Small-angle XRD patterns of the calcined MS hosts and $CaWO_4$:Tb^{3+}@MS are shown in Figure 1. Three diffraction peaks are observed in the small-angle XRD patterns of rod-like SBA-15 silica particles (R-SBA-15) and $CaWO_4$:Tb^{3+}@R-SBA-15 (Figure 1A), which can be indexed to the (100), (110), and (200) diffractions of a 2D hexagonal mesostructure (*P6mm*), in accord with the previous reports.[8a] For spherical SBA-15 particles (S-SBA-15) (Figure 1B), the patterns of the matrix and $CaWO_4$:Tb^{3+}-loaded sample show peaks indexed as (100) reflections, indicating that these materials possesses less ordered structures.[16] The patterns of hollow mesoporous silica spheres (HMS) show a broad reflection in the range 1–2° (Figure 1C), which indicates the presence of a mesoporous structure without long-range ordering.[12c] The strong (100) peak of mesoporous silica tubes (MST) shown in Figure 1D reveals an ordered mesopore system of silica materials. The intensities of these characteristic diffraction peaks decreased significantly after the introduction of $CaWO_4$:Tb^{3+} onto the MS hosts. This could be attributed to the incorporation of $CaWO_4$:Tb^{3+} nanoparticles in the pores, which can reduce the scattering contrast between the pores and the framework of the mesoporous materials.[17] The wide-angle XRD patterns of $CaWO_4$:Tb^{3+}@MS are demonstrated in Figure 2. The broad band centered at $2\theta = 22°$ is the characteristic peak for amorphous SiO_2 (JCPDS No. 29–0085). The other diffraction peaks can be indexed to crystalline $CaWO_4$ (JCPDS No. 41–1431), suggesting that $CaWO_4$:Tb^{3+} has crystallized well on the MS particles. In general, the nanocrystallite size can be estimated from the Scherrer formula: $D = K\lambda/(\beta\cos\theta)$, where λ is the X-ray wavelength (0.15405 nm), β is the full width at half maximum (FWHM), θ is the diffraction angle, K is a constant (0.89) and D is the average grain size.[18] The strongest peak (112) at 28.68° was used to calculate the average crystallite size (D) of the $CaWO_4$:Tb^{3+} particles. The estimated sizes of $CaWO_4$:Tb^{3+} crystallites for $CaWO_4$:Tb^{3+}@HMS and $CaWO_4$:Tb^{3+}@MST are about 15 and 23 nm, respectively, which are in the 10–40 nm pore-size range of the two kinds of pristine silica. For $CaWO_4$:Tb^{3+}@S-SBA-15, the estimated average size of $CaWO_4$:Tb^{3+} crystallites is 19 nm, which is also in the range of the larger pores shown in the pore-size distribution (Figure 6B). The estimated average

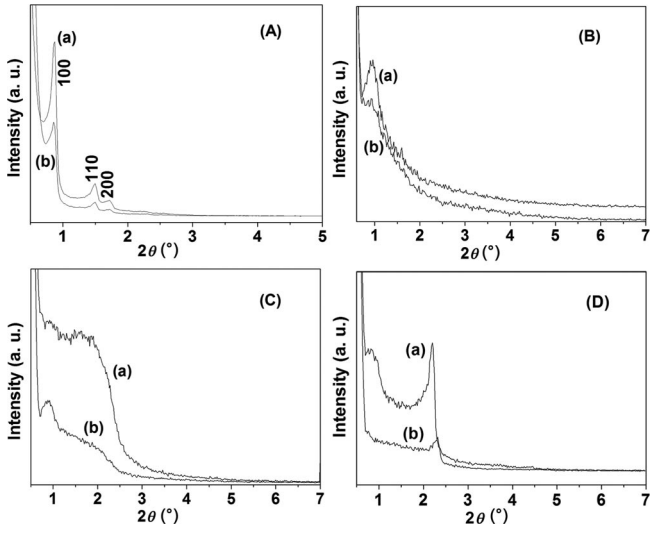

Figure 1. Small-angle XRD patterns of calcined silica (a) and $CaWO_4$:Tb^{3+}-loaded composites (b): (A) rod-like SBA-15 (R-SBA-15), (B) spherical SBA-15 (S-SBA-15), (C) hollow mesoporous silica spheres (HMS), (D) mesoporous silica tubes (MST).

Table 1. Textural parameters of calcined silica matrices, $CaWO_4$:Tb^{3+}-loaded composites, and LYZ-loaded luminescent composites at different buffer solution pH values (7.0 and 10.0). The amounts loaded and adsorbed are given in mg/g composite.

Samples	D_{pore} (nm)	Pore volume (cm^3/g)	S_{BET} (m^2/g)	$CaWO_4$:Tb^{3+} (mg/g)	Lysozyme capacity (mg/g)
R-SBA-15	8.04	1.14	566		
$CaWO_4$:Tb^{3+}@R-SBA-15	8.06	1.01	501	121.1	
LYZ@$CaWO_4$:Tb^{3+}@R-SBA-15 (pH 7.0)	7.36	0.51	275		386
LYZ@$CaWO_4$:Tb^{3+}@R-SBA-15 (pH 10.0)	5.98	0.24	160		658
S-SBA-15	15.81	2.00	505		
$CaWO_4$:Tb^{3+}@S-SBA-15	15.72	1.72	438	144.7	
LYZ@$CaWO_4$:Tb^{3+}@S-SBA-15 (pH 7.0)	10.08	0.55	290		346
LYZ@$CaWO_4$:Tb^{3+}@S-SBA-15 (pH 10.0)	7.58	0.55	219		644
HMS	8.69	1.62	746		
$CaWO_4$:Tb^{3+}@HMS	8.79	1.17	530	110.0	
LYZ@$CaWO_4$:Tb^{3+}@HMS (pH 7.0)	9.97	0.56	263		272
LYZ@$CaWO_4$:Tb^{3+}@HMS (pH 10.0)	7.15	0.47	223		571
MST	9.11	1.40	614		
$CaWO_4$:Tb^{3+}@MST	7.30	1.03	563	154.9	
LYZ@$CaWO_4$:Tb^{3+}@MST (pH 7.0)	9.92	0.72	291		233
LYZ@$CaWO_4$:Tb^{3+}@MST (pH 10.0)	9.18	0.47	203		436

crystallite size of $CaWO_4:Tb^{3+}$ is about 18 nm for $CaWO_4:Tb^{3+}$@R-SBA-15, which is larger than the average pore diameter calculated by the desorption branch of the isotherm. This can be attributed to a deviation. It can be seen that the particle sizes of some $CaWO_4:Tb^{3+}$ crystallites shown in the corresponding TEM image are smaller than the pore size of R-SBA-15. The amounts of the $CaWO_4:Tb^{3+}$ incorporated in these samples are 121.1, 144.7, 110.0, and 154.9 mg/g composite for R-SBA-15, S-SBA-15, HMS, and MST, respectively. (Table 1) The amounts loaded are determined by the morphology, the mesostructure of the silica matrices, and the stirring time during the deposition process.

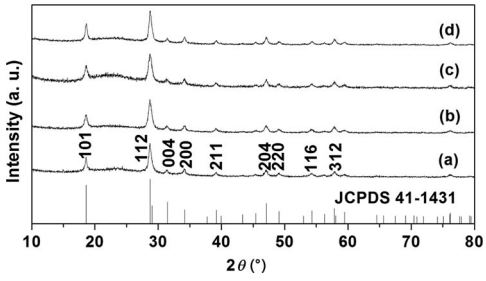

Figure 2. Wide-angle XRD patterns of $CaWO_4:Tb^{3+}$-loaded composites: (a) $CaWO_4:Tb^{3+}$@R-SBA-15, (b) $CaWO_4:Tb^{3+}$@S-SBA-15, (c) $CaWO_4:Tb^{3+}$@HMS, (d) $CaWO_4:Tb^{3+}$@MST and the standard data for $CaWO_4$ (JCPDS No. 41–1431).

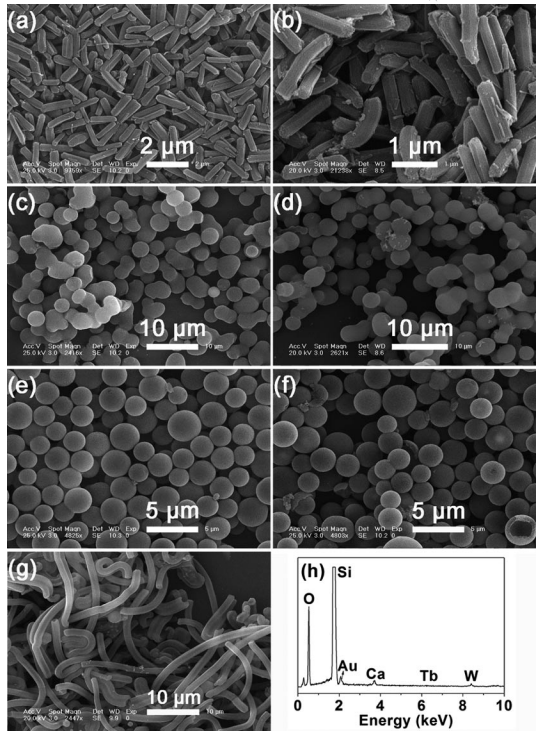

Figure 3. SEM images of calcined silica and $CaWO_4:Tb^{3+}$-loaded samples: (a) R-SBA-15, (b) $CaWO_4:Tb^{3+}$@R-SBA-15, (c) S-SBA-15, (d) $CaWO_4:Tb^{3+}$@ S-SBA-15, (e) HMS, (f) $CaWO_4:Tb^{3+}$@HMS, (g) $CaWO_4:Tb^{3+}$@MST; (h) EDX spectrum of $CaWO_4:Tb^{3+}$@R-SBA-15.

SEM and TEM

The morphologies of the MS matrices and $CaWO_4:Tb^{3+}$@MS are illustrated in the SEM images shown in Figure 3. The R-SBA-15 prepared without the swelling agent TMB consists of rod-like particles with length of 1–2 μm. The S-SBA-15 synthesized with TMB exhibits spherical morphology with diameter in 2–4 μm. Spherical particles with diameter of 2–4 μm were obtained when 9.0 mL of ethyl acetate used. The broken hollow sphere can be clearly seen in Figure 3f, with the shell thickness of ca. 400 nm. The silica tube comprises particles with average diameter about 2 μm and length varying from 10 to 50 μm. The energy dispersive X-ray (EDX) analysis of these composites in Figure 3h shows that these composites are composed of Si, O, Ca, W and Tb elements, respectively.

TEM images of the two kinds of $CaWO_4:Tb^{3+}$-loaded SBA-15-type composites show ordered arrays of mesopore as those bare hosts, confirming that highly ordered mesopores are stable during the process of luminescence-functionalization of silica matrices. The SEM and TEM images of the silica spheres and tubes shown in Figures 3 and 4 confirm their hollowness. The crystals of $CaWO_4:Tb^{3+}$ are seen as black dots dispersed in the pore and on the outer surface of the silica materials. The TEM images also display the aggregates of $CaWO_4:Tb^{3+}$ crystals on the outer surface of the silica.

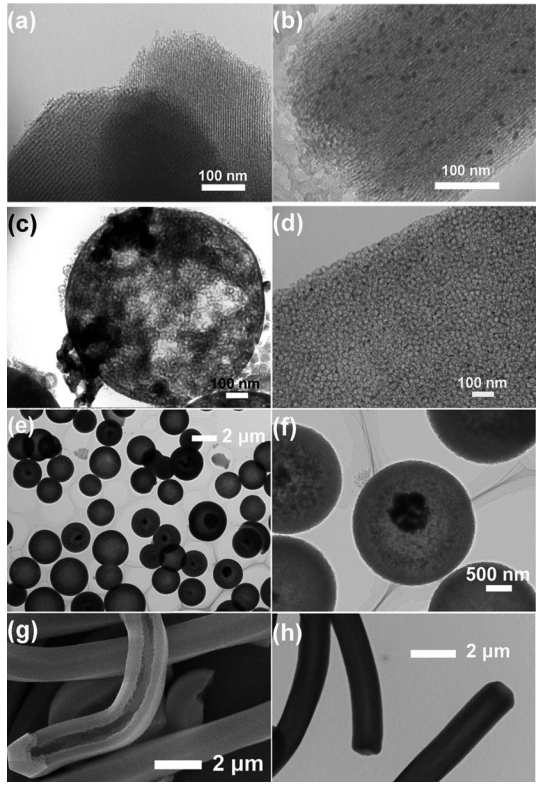

Figure 4. Images of calcined silica and $CaWO_4:Tb^{3+}$-loaded samples: (a) R-SBA-15 (TEM), (b) $CaWO_4:Tb^{3+}$@R-SBA-15 (TEM), (c, d) $CaWO_4:Tb^{3+}$@S-SBA-15 (TEM), (e, f) $CaWO_4:Tb^{3+}$@HMS (TEM), (g) MST (SEM), (h) MST (TEM).

N_2 Adsorption/Desorption

The N_2 adsorption/desorption isotherms and pore-size distributions of the composites before and after loading with different amounts of LYZ (at solution pH values of 7.0 and 10.0) are shown in Figures 5 and 6. SBA-15-type silica hosts and $CaWO_4$:Tb^{3+}-loaded composites have a type IV isotherm with H1 hysteresis loops, which is characteristic of porous materials with cylindrical channels. The narrow and sharp pore-size-distribution curves [Figure 6 (A, B)] reveal that SBA-15-type composites have highly uniform pore size. The isotherms of HMS, MST, and the corresponding $CaWO_4$:Tb^{3+}-loaded composites all show type IV isotherms and pronounced hysteresis loops. For HMS, the pore-size distributions show peaks in the range 2–4 nm, together with a broad peak in the range 10–40 nm. The pore-size distributions for MST have peaks similar to those of HMS. These results suggest that the pores of the obtained luminescent HMS and MST composites are less ordered relative to those of SBA-15-type samples.

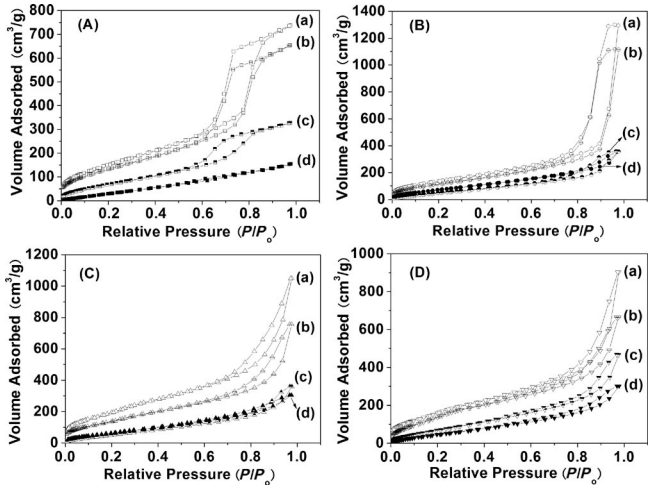

Figure 5. N_2 adsorption/desorption isotherms of calcined silica (a), $CaWO_4$:Tb^{3+}-loaded composites (b), luminescent composites loaded with LYZ at pH 7.0 (c), and pH 10.0 (d). (A) R-SBA-15, (B) S-SBA-15, (C) HMS, (D) MST.

The textural parameters of the silica hosts as well as those of $CaWO_4$:Tb^{3+}@MS are presented in Table 1. The surface area and pore volume of the MS matrices decrease after the introduction of $CaWO_4$:Tb^{3+} nanoparticles. However, the synthesized luminescent composites still have high BET surface area, large pore volume ($>1.0\ cm^3/g$), and pore size suitable for the entrapment of LYZ molecules.

It can be seen that the pore volume and surface area decrease markedly after the adsorption of LYZ molecules, which can be attributed to the tight packing of lysozyme molecules into the pores of $CaWO_4$:Tb^{3+}-loaded mesoporous silica.[10f] $CaWO_4$:Tb^{3+}@R-SBA-15 immobilized with LYZ exhibits a type IV isotherm with a smaller H1 hysteresis loop after adsorption at a solution pH value of 7.0. The adsorption isotherm for $CaWO_4$:Tb^{3+}@R-SBA-15 at pH 10.0 is more like the type II isotherm of the IUPAC classification. The other composites loaded with LYZ show type

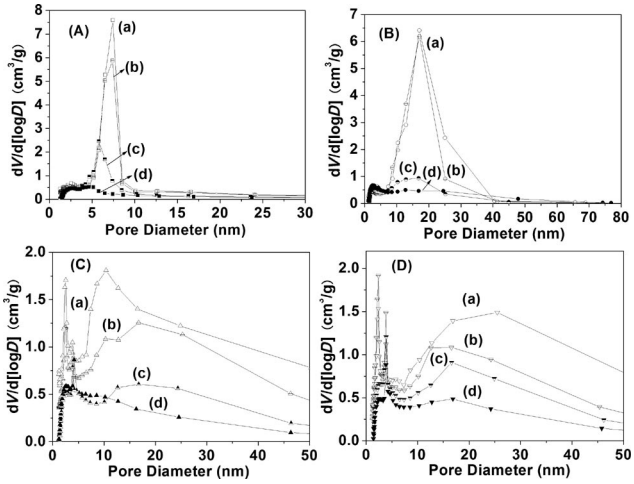

Figure 6. Pore-size distributions of calcined silica (a), $CaWO_4$:Tb^{3+}-loaded composites (b), luminescent composites loaded with LYZ at pH 7.0 (c), and pH 10.0 (d). (A) R-SBA-15, (B) S-SBA-15, (C) HMS, (D) MST. Pore-size distribution was calculated from the desorption branch of the isotherm by the BJH method.

IV isotherms with hysteresis loops that are smaller at pH 10.0 than at pH 7.0. The amount of N_2 adsorbed for the composites decreases with the increase in the immobilized amount of LYZ. These pieces of evidence further confirm that the mesopores are filled with LYZ molecules.

Lysozyme Immobilization and Release

Figure 7 shows the rate of adsorption of LYZ of the synthesized composites. The morphologies, particle size, textural properties of MS composites, and the solution pH play important roles in the adsorption of enzyme. The adsorption reaches equilibrium in 48 h at pH 7.0, while 96 h are needed at pH 10.0. It can be seen that these composites demonstrate various adsorption capacities. $CaWO_4$:Tb^{3+}@R-SBA-15, which possesses an average pore diameter of 8.06 nm, BET surface of 501 m^2/g, and pore volume of 1.01 cm^3/g, shows the largest adsorption at both pH values: 386 mg/g at pH 7.0 and 658 mg/g at pH 10.0. For $CaWO_4$:Tb^{3+}@S-SBA-15, which has a mean pore diameter of 15.72 nm, BET surface of 438 m^2/g, and pore volume of 1.72 cm^3/g, the equilibrium capacity of LYZ is 346 mg/g at pH 7.0 and 644 mg/g at pH 10.0, which is close to that of $CaWO_4$:Tb^{3+}@R-SBA-15. The amount of LYZ adsorbed onto $CaWO_4$:Tb^{3+}@S-SBA-15 reaches its largest value in 30 min at both solution pH values. However, $CaWO_4$:Tb^{3+}@HMS, which exhibits a spherical morphology similar to that of $CaWO_4$:Tb^{3+}@S-SBA-15, has a relatively lower adsorption amount of 272 mg/g at pH 7.0 and 571 mg/g at pH 10.0, relative to the SBA-15 system. This can be ascribed to the les ordered mesopores of the silica. Meanwhile, a small part of the broken sphere may decrease the amount of lysozyme taken up. $CaWO_4$:Tb^{3+}@MST exhibits the lowest adsorption capacity among these samples: 233 mg/g at pH 7.0 and

436 mg/g at pH 10.0. This can be attributed to its large particle size, which may be not favorable for the diffusion of the enzyme molecules into the mesopores.[19]

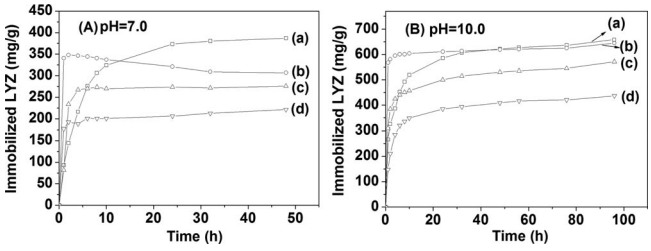

Figure 7. LYZ adsorption curves of luminescent composites at pH 7.0 (A), 10.0 (B): (a) $CaWO_4$:Tb^{3+}@R-SBA-15, (b) $CaWO_4$:Tb^{3+}@S-SBA-15, (c) $CaWO_4$:Tb^{3+}@HMS, (d) $CaWO_4$:Tb^{3+}@MST.

It can be seen that the adsorbed amounts at equilibrium are significantly affected by the pH of the buffer solution and the maximum adsorbed amounts of lysozyme on the composites at pH 10.0 are much larger than the adsorbed amounts at pH 7.0. At pH 10.0, which is near the pI of lysozyme (≈11), the net charge of the lysozyme is low. The repulsion between the amino acid residues on the surface of lysozyme molecules is very small, thus the lysozyme molecules can pack closely on the adsorbent surface and the monolayer adsorbing capacity is large. Moreover, although the overall net charge for proteins is low near the pI value, there still exist positively (or negatively) charged regions on the protein surface, and the negatively charged silanols (silica, pI ≈ 2–3) have strong electrostatic interaction with polar and positively charged regions of the lysozyme molecules.[10f,11d] In contrast, at pH 7.0, the amino acids in the protein have strong positive charges, lateral repulsion between the neighboring lysozyme molecules is strong, and the molecule size of lysozymes is large, so the amounts adsorbed at pH 7.0 are smaller than those at pH 10.0.

Figure 8 shows the cumulative release profiles of lysozymes from these enzyme-loaded composites (adsorbed at a solution pH of 10.0) in buffer solution with pH 7.0 with shaking. These composites show a two-step release pattern with initial burst release and subsequent relatively slow sustained release. The initial burst release is due to the protein molecules adsorbed to the exterior surface and near the entrance of the channels. As a great amount of lysozyme molecules enter into the mesopores, the entrapped proteins are released slowly for a long period. $CaWO_4$:Tb^{3+}@S-SBA-15 with largest mean pore size shows the fastest release rate; the amount of released lysozyme reaches 30.44% in the first 30 min, whereas the initial burst release rates are 11.06%, 19.40%, and 21.94% for $CaWO_4$:Tb^{3+}-loaded R-SBA-15, HMS, and MST, respectively. The total amount of LYZ released from $CaWO_4$:Tb^{3+}@R-SBA-15 reaches 32.97% after 36 h.

To analyze the structural stability of the immobilized lysozymes, the FTIR spectra of the free lysozymes and luminescent composites loaded with lysozyme were recorded

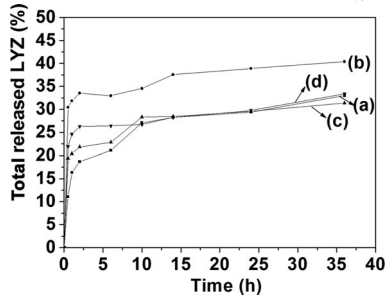

Figure 8. The releasing profiles of: (a) LYZ@$CaWO_4$:Tb^{3+}@R-SBA-15, (b) LYZ@$CaWO_4$:Tb^{3+}@S-SBA-15, (c) LYZ@$CaWO_4$:Tb^{3+}@HMS, (d) LYZ@$CaWO_4$:Tb^{3+}@MST.

(Figure 9). As the spectra of the four kinds of silica composites are similar, only the spectra for R-SBA-15, $CaWO_4$:Tb^{3+}@R-SBA-15, and the LYZ-loaded samples are shown. For the silica matrix, absorption bands due to OH (3430 cm^{-1}), H_2O (1630 cm^{-1}), Si–O–Si (ν_{as}, 1083 cm^{-1}; ν_s, 805 cm^{-1}), Si–OH (ν_s, 960 cm^{-1}), and Si–O (δ, 460 cm^{-1}) bonds (where ν_{as}, and ν_s, and δ indicate asymmetric stretching, symmetric stretching, and bending, respectively) are observed.[20] For the $CaWO_4$:Tb^{3+}-loaded sample (Figure 9b), the W–O band at 816 cm^{-1} for $CaWO_4$:Tb^{3+} crystals can be observed clearly. The FTIR spectra further confirm that $CaWO_4$:Tb^{3+} has crystallized well on the mesoporous silica, which is consistent with the XRD results. The spectrum of the free lysozyme exhibits two characteristic peaks at approximate values of 1650 and 1530 cm^{-1}, denoted as amide bands I and II. Amide band I (near 1650 cm^{-1}) is due to the C=O stretching mode, whereas amide band II (near 1530 cm^{-1}) is ascribed to the bending and the stretching modes of the N–H and C–N vibrations, respectively. It has been reported that proteins having an α-helical conformation show strong amide I bands near 1650 cm^{-1}. Thus the band observed in Figure 9c, d at 1656 cm^{-1} is due to the α-helical conformation of the LYZ molecule.[10f,21] The strong amide II band at 1542 cm^{-1} is due to the parallel β-sheet structure of LYZ.[10f,21] The bands near 1456 and 1401 cm^{-1} are assigned to the CH_2 and CH_3 stretching modes of the aliphatic moieties of the amino acid side chains. These bands appear in the spectra

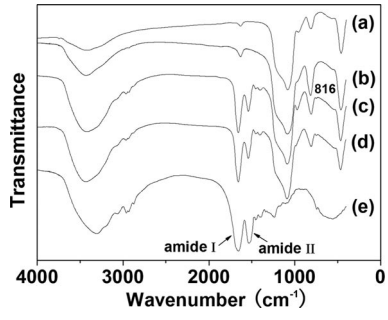

Figure 9. FTIR spectra of (a) R-SBA-15, (b) $CaWO_4$:Tb^{3+}@R-SBA-15, (c) LYZ@$CaWO_4$:Tb^{3+}@R-SBA-15 (pH 7.0), (d) LYZ@$CaWO_4$:Tb^{3+}@R-SBA-15 (pH 10.0), (e) LYZ.

of lysozyme-loaded $CaWO_4:Tb^{3+}$@MS, which indicates that the structural conformation of LYZ is retained after immobilization.

Photoluminescence Properties

The photographs of LYZ-loaded $CaWO_4:Tb^{3+}$@R-SBA-15 luminescent composites under UV irradiation (254 nm) are illustrated in the inset of Figure 10A. Green luminescence can be observed from $CaWO_4:Tb^{3+}$@R-SBA-15 (photograph a), further revealing the successful incorporation of $CaWO_4:Tb^{3+}$ crystals in the mesoporous silica. Though the photoluminescence (PL) intensity of the composite decreased after the immobilization of lysozyme, the green luminescence can still be observed clearly (photograph b), demonstrating the good stability of the adsorbent.

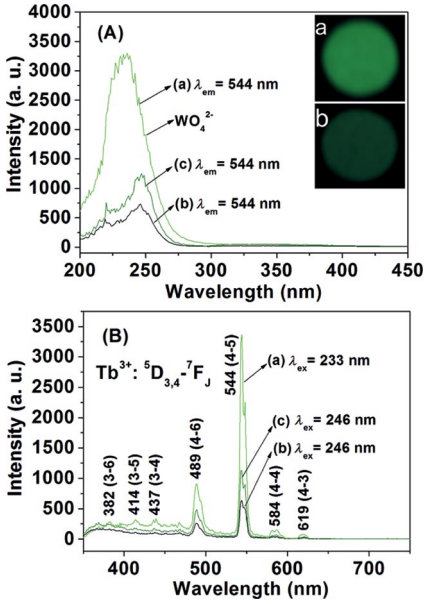

Figure 10. PL excitation (A) and emission (B) spectra of $CaWO_4:Tb^{3+}$@R-SBA-15 (a), LYZ@$CaWO_4:Tb^{3+}$@R-SBA-15 (pH 10.0) (b), LYZ@$CaWO_4:Tb^{3+}$@R-SBA-15 (after release for 36 h) (c). Inset: photographs of $CaWO_4:Tb^{3+}$@R-SBA-15 (a) and LYZ@$CaWO_4:Tb^{3+}$@R-SBA-15 (pH 7.0) (b) under UV lamp irradiation (254 nm).

For the $CaWO_4:Tb^{3+}$-functionalized composites, the excitation spectrum (monitored by the Tb^{3+} $^5D_4$–$^7F_5$ transition at 544 nm) consists of a narrow band with maximum at 233 nm, which corresponds to the charge transfer transition in WO_4^{2-} groups in which an oxygen 2p electron goes into empty tungsten 5d orbital.[22] Upon excitation of WO_4^{2-} at 233 nm, the obtained emission spectrum (Figure 10B) contains exclusively the characteristic emission of Tb^{3+}, with $^5D_4$–$^7F_5$ green emission (544 nm) as the most prominent group (other transitions are labeled inside Figure 10B). The blue emission from WO_4^{2-} is nearly undetected, suggesting that an efficient energy transfer from WO_4^{2-} to Tb^{3+} has occurred in the $CaWO_4:Tb^{3+}$ crystals. Furthermore, the emission from the $^5D_3$ level of Tb^{3+} is much weaker than that from the $^5D_4$ level due to the cross relaxation effect of Tb^{3+}.[23] The PL intensity of $CaWO_4:Tb^{3+}$@MS decreases dramatically after adsorption of lysozyme, while it increases again with the release of LYZ molecules [Figure 10A, B (b)(c)]. As shown in Figure 10A, the maximum of the excitation spectrum shifts to 246 nm after LYZ immobilization. Lysozyme, with molecular mass of 14400 Da, has a single peptide chain of a total of 129 amino acids containing a high proportion of lysine and arginine.[10f,24] These amino acid residues comprise a great amount of organic groups such as CH_2, CH_3, and amide, which produce high-energy vibrational modes that could strongly quench the excited state of the Tb^{3+} ion through multiphonon relaxation.[25] With the desorption and diffusion of the LYZ molecules from the luminescent composites to the buffer solution, the quenching effect on the emission of Tb^{3+} will be weakened, leading to an increase in the emission intensity. As shown in Figure 11, the PL emission intensity of Tb^{3+} in $CaWO_4:Tb^{3+}$@R-SBA-15 (defined as the integrated area intensity of $^5D_4$–^7F_J of Tb^{3+}) increases with the increase in the total amount of LYZ molecules released. This indicates that the release of the enzyme can be tracked by the change in the luminescence of the $CaWO_4:Tb^{3+}$ incorporated in the mesoporous silica, which would provide a promising vector for large biomolecules.

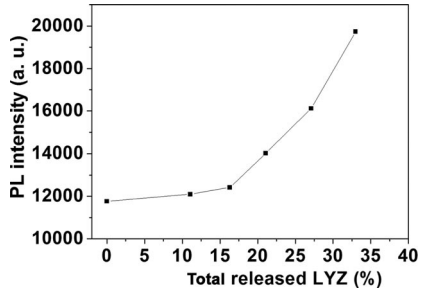

Figure 11. The PL emission intensity of Tb^{3+} in $CaWO_4:Tb^{3+}$@R-SBA-15 as a function of total amount of lysozyme released.

Conclusions

MS materials with various regular morphologies were luminescence-functionalized by deposition of $CaWO_4:Tb^{3+}$ nanocrystals onto them by a Pechini sol–gel process. These luminescent composites still possess suitable pore size, high surface area, and large pore volume for lysozyme immobilization after the incorporation of $CaWO_4:Tb^{3+}$ nanoparticles. Furthermore, these composites exhibit strong green emission under UV lamp irradiation (254 nm). These composites show various lysozyme adsorption capacities in buffer solutions with different pH values. $CaWO_4:Tb^{3+}$@R-SBA-15 reveals a maximum equilibrium adsorption amount at solution pH 7.0 and 10.0. $CaWO_4:Tb^{3+}$@S-SBA-15 shows high adsorption amounts and the fastest release rate. The amounts of LYZ adsorbed on luminescence-functionalized HMS and MST were lower than that adsorbed onto SBA-15-type composites. The adsorption behavior was affected by the morphology, particle size, the mesopore struc-

ture of the adsorbent, and the pH value of the buffer solution. The emission intensity of Tb^{3+} in $CaWO_4$:Tb^{3+}@R-SBA-15 increases with the increase in the total amount of LYZ molecules released, which enables the lysozyme release to be tracked by the change in the luminescence intensity.

Experimental Section

Materials and Synthesis

Materials: All the chemicals were of analytical reagent grade (A. R.) and were used directly without further purification: tetraethoxysilane (TEOS, Yili Fine Chemical Co., Beijing), $(EO)_{20}(PO)_{70}(EO)_{20}$ (P123, *M*w = 5800, Aldrich), cetyltrimethylammonium bromide (C_{16}TABr, Yili Fine Chemical Co., Beijing), sodium silicate ($Na_2SiO_3{\cdot}9H_2O$, molar ratio Na_2O/SiO_2 = 1.03, Beilian Fine Chemical Co., Tianjing), ethyl acetate ($CH_3COOC_2H_5$, Beijing Chemical Reagent Company, Beijing), 1,3,5-trimethylbenzene (TMB, Sinopharm Chemical Reagent Co., Ltd.).

Synthesis of Mesoporous Silica Matrices: Rod-like SBA-15 silica particles (R-SBA-15) were synthesized according to a published process.[26] Spherical SBA-15 particles (S-SBA-15) were synthesized on the basis of a previous report.[8a] Mesoporous silica tubes (MST) and hollow mesoporous silica spheres (HMS) were synthesized on the basis of the previous literature with some modification.[27] A total of C_{16}TABr (5.03 g) followed by $Na_2SiO_3{\cdot}9H_2O$ (5.97 g) were dissolved in distilled water (90 mL) at 30 °C. After the mixture became a clear solution, a certain amount of ethyl acetate was quickly added whilst stirring. The amounts of ethyl acetate were 6.0 mL for MST and 9.0 mL for HMS. After being stirred for 30 s, the mixture was allowed to stand at 20 °C for 5 h. Then the mixture was kept in a conical flask at 90 °C for 3 d in an oven. During the aging process, organic vapor was allowed to escape through the cap of the flask. The resulting solid was recovered, washed, and dried at ambient temperature. The template was removed by calcination at 600 °C for 6 h in flowing air.

Synthesis of $CaWO_4$:Tb^{3+}@MS Composites: The $CaWO_4$:Tb^{3+}@MS composites were prepared by a Pechini sol–gel process, the doping concentration of Tb^{3+} was 5 mol-% of Ca^{2+} in $CaWO_4$, which had been optimized previously.[28] $CaCO_3$ (0.19 g) and Tb_4O_7 (0.0187 g, with purity > 99.99%, Science and Technology Parent Company of Changchun Institute of Applied Chemistry, China) was dissolved in dilute HNO_3 whilst stirring, and the superfluous HNO_3 was driven off until the pH of the solution reached a value between two and three. The as-prepared $Ca(NO_3)_2$ was mixed with ammonium(meta) tungstate hydrate (0.5494 g, $H_{26}N_6O_{41}W_{12}{\cdot}18H_2O$, Fluka), water/ethanol solution (20 mL, 15:5 v/v) containing citric acid monohydrate (0.8406 g) as a chelating agent for the metal ions. The molar ratio of metal ions to citric acid was 1:2. As a cross-linking agent, polyethylene glycol (PEG, molecular weight = 10000) was added with a final concentration of 0.20 g/mL. The solution was stirred for 1 h to form a sol, and then the MS particles were added whilst stirring. The silica particles were separated by centrifugation after the suspension was stirred for 4 h. For HMS particles, the stirring time was reduced to 2 h to prevent the cracking of spheres. The samples were immediately dried at 100 °C for 1 h. Then, the dried samples were heated to 600 °C with a heating rate of 1 °C/min, and held at this temperature for 2 h in air.

Immobilization of LYZ to Luminescent Composites: For lysozyme immobilization, $CaWO_4$:Tb^{3+}@MS (200 mg) was suspended in a solution (1.0 mg/mL) of lysozyme from chicken egg white (200 mL, L6876, Sigma) in a covered vessel to prevent evaporation. phosphate buffer solution (50 mM, pH 7.0) and borax/NaOH buffer solution (50 mM, pH 10.0) were used as the buffer solutions during protein adsorption. The resulting mixture was continuously shaken at 20 °C until equilibrium was reached. Samples were withdrawn periodically for immediate UV/Vis analysis and then returned to the mixture. The amount of LYZ immobilized was calculated by subtracting the amount found in the supernatant liquid after adsorption from the amount of LYZ present before addition of the adsorbent by UV absorption at 281 nm. After the adsorption equilibrium, the solid was collected, freeze-dried, and stored at room temperature in a desiccator for further use.

Release Experiment: The enzyme-loaded sample was dispersed in phosphate buffer solution (50 mM, pH 7.0). The obtained suspension was shaken at room temperature for a certain time. The protein content of the solution was measured by using UV/Vis absorption. The percentage of total released enzyme from the composites was then calculated from these enzyme content data.

Characterization: X-ray power diffraction (XRD) was performed with a Rigaku-Dmax 2500 diffractometer using Cu-K_α radiation (λ = 0.15405 nm). Fourier-transform infrared (FTIR) spectra were recorded with a Bruker Vertex 70 IR spectrophotometer by the KBr pellet technique. N_2 adsorption/desorption isotherms were obtained at 77 K with a NOVA-1000 apparatus. The specific surface areas were calculated by the Brunauer–Emmett–Teller (BET) method, and the pore-size distributions were derived from desorption branches of the isotherms by the Barrett–Joyner–Halenda (BJH) method. The morphology of the samples was inspected by using a field emission scanning electron microscope (FESEM, XL30, Philips) equipped with an energy-dispersive X-ray spectrum (EDX, JEOL JXA-840). Transmission electron microscopy (TEM) was performed with a FEI Tecnai G2 S-Twin transmission electron microscope with a field emission gun operating at 200 kV. Inductively coupled plasma (ICP) measurements (Thermo iCAP 6000 ICP-OES) were performed on the sample to determine the exact loading level of $CaWO_4$:Tb^{3+}. The photoluminescence (PL) measurements were performed with a Hitachi F-4500 spectrophotometer equipped with a 150 W xenon lamp as the excitation source. The UV/Vis absorption spectra values were measured with a TU-1901 spectrophotometer.

Acknowledgments

This project is financially supported by the National Basic Research Program of China (2007CB935502, 2010CB327704) and the National Natural Science Foundation of China (NSFC 60977013, 20901074, 50872131).

[1] a) D. Avnir, S. Braun, O. Lev, M. Ottolenghi, *Chem. Mater.* **1994**, *6*, 1605–1614; b) B. D. Martin, B. P. Gaber, C. H. Patterson, D. C. Turner, *Langmuir* **1998**, *14*, 3971–3975; c) W. Inglis, G. H. Sanders, P. M. Williamsan, M. C. Davies, C. J. Roberts, S. J. B. Tendler, *Langmuir* **2001**, *17*, 7402–7405; d) D. L. Shi, *Adv. Funct. Mater.* **2009**, *19*, 3356–3373.
[2] H. H. Weetall, *Appl. Biochem. Biotechnol.* **1993**, *41*, 157–188.
[3] D.-S. Jiang, S.-Y. Long, H.-Y. Xiao, J.-Y. Zhou, *Biochem. Eng. J.* **2005**, *25*, 15–23.
[4] a) J. Wang, *Anal. Chim. Acta* **1999**, *399*, 21–27; b) B. Wang, J. Zhang, G. Cheng, S. Dong, *Anal. Chim. Acta* **2000**, *407*, 111–118.
[5] R. M. Greer, B. A. Scruggs, R. A. May, B. D. Chandler, *Langmuir* **2009**, *25*, 7161–7168.
[6] a) A. Vinu, M. Miyahara, K. Ariga, *J. Phys. Chem. B* **2005**, *109*, 6436–6441; b) M. Hartmann, A. Vinu, G. Chandrasekar, *Chem. Mater.* **2005**, *17*, 829–833.

[7] a) M. Miyazaki, J. Kaneno, M. Uehara, M. Fuji, H. Shimizu, *Chem. Commun.* **2003**, *5*, 648–649; b) A. M. Klibanov, *Science* **1983**, *219*, 722–727; c) T. Zoungrana, G. H. Findenegg, W. Norde, *J. Colloid Interface Sci.* **1997**, *190*, 437–448; d) H. Takahashi, B. Li, T. Sasaki, C. Miyazaki, T. Kajino, S. Inagaki, *Chem. Mater.* **2000**, *12*, 3301–3305; e) H. Takahashi, B. Li, T. Sasaki, C. Miyazaki, T. Kajino, S. Inagaki, *Microporous Mesoporous Mater.* **2001**, *44–45*, 755–762.

[8] a) D. Y. Zhao, Q. S. Huo, J. L. Feng, B. F. Chmelka, G. D. Stucky, *J. Am. Chem. Soc.* **1998**, *120*, 6024–6036; b) D. Y. Zhao, J. L. Feng, Q. S. Huo, N. Melosh, G. Fredrikson, B. Chmelka, G. D. Stucky, *Science* **1998**, *279*, 548–552; c) P. D. Yang, D. Y. Zhao, D. I. Margolese, B. F. Chmelka, G. D. Stucky, *Nature* **1998**, *396*, 152–155; d) X. Roy, M. J. Maclachlan, *Chem. Eur. J.* **2009**, *15*, 6552–6559.

[9] J. Deere, E. Magner, J. G. Wall, B. K. Hodnett, *Chem. Commun.* **2001**, 465–466.

[10] a) J. F. Díaz, K. J. Balkus Jr., *J. Mol. Catal. B* **1996**, *2*, 115–126; b) M. Hartmann, *Chem. Mater.* **2005**, *17*, 4577–4593; c) A. Katiyar, S. Yadav, P. G. Smirniotis, N. G. Pinto, *J. Chromatogr. A* **2006**, *1122*, 13–20; d) J. Fan, J. Lei, L. M. Wang, C. Z. Yu, B. Tu, D. Y. Zhao, *Chem. Commun.* **2003**, 2140–2141; e) J. M. Sun, H. Zhang, R. J. Tian, D. Ma, X. H. Bao, D. S. Su, H. F. Zou, *Chem. Commun.* **2006**, 1322–1324; f) A. Vinu, M. Murugsan, *J. Phys. Chem. B* **2004**, *108*, 7323–7330.

[11] a) Y. J. Wang, F. Caruso, *Chem. Mater.* **2005**, *17*, 953–961; b) M. Park, S. S. Park, M. Selvaraj, D. Y. Zhao, C.-S. Ha, *Microporous Mesoporous Mater.* **2009**, *124*, 76–83; c) S. C. Shen, P. C. Chow, S. Kim, K. Zhu, R. B. H. Tan, *J. Colloid Interface Sci.* **2008**, *321*, 365–372; d) S. Z. Qiao, H. Djojoputro, Q. H. Hu, G. Q. Lu, *Prog. Solid State Chem.* **2006**, *34*, 249–256.

[12] a) T. Valdés-Solís, A. F. Rebolledo, M. Sevilla, P. Valle-Vigón, O. Bomatí-Miguel, A. B. Fuertes, P. Tartaj, *Chem. Mater.* **2009**, *21*, 1806–1814; b) Y. G. Wang, J. W. Ren, X. H. Liu, Y. Q. Wang, Y. Guo, Y. L. Guo, G. Z. Lu, *J. Colloid Interface Sci.* **2008**, *326*, 158–165; c) Y. F. Zhu, S. Kaskel, J. L. Shi, T. Wage, K.-H. V. Pée, *Chem. Mater.* **2007**, *19*, 6408–6413.

[13] a) A. C. Ferrand, D. Imbert, A. S. Chauvin, C. D. B. Vandevyver, J.-C. G. Bünzlin, *Chem. Eur. J.* **2007**, *13*, 8678–8687; b) J.-C. G. Bünzlin, C. Piguet, *Chem. Soc. Rev.* **2005**, *34*, 1048–1077; c) I. Hemmilä, V. M. Mukkala, *Crit. Rev. Clin. Lab. Sci.* **2001**, *38*, 441–519; d) S. Faulkner, J. L. Matthews in *Comprehensive Coordination Chemistry II, Vol. 9* (Ed.: M. D. Ward), Elsevier Pergamon, Amsterdam, **2004**, pp. 913–944.

[14] a) P. P. Yang, Z. W. Quan, L. L. Lu, S. S. Huang, J. Lin, *Biomaterials* **2008**, *29*, 692–702; b) P. P. Yang, Z. W. Quan, L. L. Lu, S. S. Huang, J. Lin, H. G. Fu, *Nanotechnology* **2007**, *18*, DOI: 10.1088/0957-4484/18/23/235703 (10 pp.); c) P. P. Yang, S. S. Huang, D. Y. Kong, J. Lin, H. G. Fu, *Inorg. Chem.* **2007**, *46*, 3203–3211; d) P. P. Yang, Z. W. Quan, C. X. Li, H. Z. Lian, S. S. Huang, J. Lin, *Microporous Mesoporous Mater.* **2008**, *116*, 524–531; e) J. Sauer, F. Marlow, B. Spliethoff, F. Schüth, *Chem. Mater.* **2002**, *14*, 217–224; f) L. N. Sun, H. J. Zhang, C. Y. Peng, J. B. Yu, Q. G. Meng, L. S. Fu, F. Y. Liu, X. M. Guo, *J. Phys. Chem. B* **2006**, *110*, 7249–7258; g) C. Y. Peng, H. J. Zhang, J. B. Yu, Q. G. Meng, L. S. Fu, H. R. Li, X. M. Guo, *J. Phys. Chem. B* **2005**, *109*, 15278–15287; h) W. Xu, D. L. Akins, *J. Phys. Chem. B* **2002**, *106*, 1991–1994; i) L. D. Carlos, R. A. S. Ferreira, V. Z. Bermudez, S. J. L. Ribeiro, *Adv. Mater.* **2009**, *21*, 509–534; j) Y.-J. Li, B. Yan, *Inorg. Chem.* **2009**, *48*, 8276–8285.

[15] a) R. Ghosh, Z. F. Cui, *Biotechnol. Bioeng.* **2000**, *68*, 191–203; b) T. Arai, W. Norde, *Colloids Surf.* **1990**, *51*, 1–15; c) G. Jackler, R. Steitz, G. Jackler, C. Czeslik, *Langmuir* **2002**, *18*, 6565–6570; d) T. J. Su, J. R. Lu, R. K. Thomas, Z. F. Cui, J. Penfold, *J. Colloid Interface Sci.* **1998**, *203*, 419–429; e) Q. G. Xiao, X. Tao, H. K. Zou, J. F. Chen, *Chem. Eng. J.* **2008**, *137*, 38–44; f) M. Tortajada, D. Ramon, D. Beltran, P. Amoros, *J. Mater. Chem.* **2005**, *15*, 3859–3868.

[16] T. Yokoi, H. Yoshitake, T. Tatsumi, *J. Mater. Chem.* **2004**, *14*, 951–957.

[17] a) H. Winkler, A. Birkner, V. Hagen, I. Wolf, R. Schmechel, H. Von Seggern, R. A. Fischer, *Adv. Mater.* **1999**, *11*, 1444–1448; b) W. H. Zhang, J. L. Shi, H. R. Chen, Z. L. Hua, D. S. Yan, *Chem. Mater.* **2001**, *13*, 648–654; c) C. Y. Lai, B. G. Trewyn, D. M. Jeftinija, K. Jeftinija, S. Xu, S. Jeftinija, V. S. Y. Lin, *J. Am. Chem. Soc.* **2003**, *125*, 4451–4459.

[18] L. S. Birks, H. Friedman, *J. Appl. Phys.* **1946**, *17*, 687–692.

[19] J. Lei, J. Fan, C. Z. Yu, L. Y. Zhang, S. Y. Jiang, B. Tu, D. Y. Zhao, *Microporous Mesoporous Mater.* **2004**, *73*, 121–128.

[20] a) M. Yu, J. Lin, J. Fang, *Chem. Mater.* **2005**, *17*, 1783–1791; b) M. Yu, J. Lin, Z. Wang, J. Fu, S. Wang, H. J. Zhang, Y. C. Han, *Chem. Mater.* **2002**, *14*, 2224–2231.

[21] S. Adams, A. M. Higgins, R. A. L. Jones, *Langmuir* **2002**, *18*, 4854–4861.

[22] M. J. Treadaway, R. C. Powell, *J. Chem. Phys.* **1974**, *61*, 4003–4011.

[23] a) P. A. M. Berdowski, M. J. J. Lammers, G. Blasse, *Chem. Phys. Lett.* **1985**, *113*, 387–390; b) D. J. Robbins, B. Cockayne, B. Lent, J. L. Glasper, *Solid State Commun.* **1976**, *20*, 673–676.

[24] a) R. E. Canfield, *J. Biol. Chem.* **1963**, *238*, 2698–2707; b) J. Jollès, J. Jauregui-Adell, I. Bernier, P. Jollès, *Biochim. Biophys. Acta* **1963**, *78*, 668–689; c) R. E. Canfield, A. K. Liu, *J. Biol. Chem.* **1965**, *240*, 1997–2002.

[25] G. Blasse, B. C. Grabmaier in *Luminescent Materials*, Springer, Berlin, **1994**, pp. 74–75.

[26] A. Sayari, B. H. Han, Y. Yang, *J. Am. Chem. Soc.* **2004**, *126*, 14348–14349.

[27] G. Schulz-Ekloff, J. Rathouský, A. Zukal, *Int. J. Inorg. Mater.* **1999**, *1*, 97–102.

[28] a) J. Lin, M. Yu, C. K. Lin, X. M. Liu, *J. Phys. Chem. C* **2007**, *16*, 5835–5845; b) P. Y. Jia, X. M. Liu, G. Z. Li, M. Yu, J. Fang, J. Lin, *Nanotechnology* **2006**, *17*, 734–742.

Received: February 1, 2010
Published Online: May 19, 2010

